HOKKAIDO UNIVERSITY

Title	Decoding multiple source signatures in coseismic ionospheric disturbances of the 2024 January Mw7.5 Noto-Peninsula earthquake, Central Japan
Author(s)	Heki, Kosuke
Citation	Earth and Planetary Science Letters, 640, 118796 https://doi.org/10.1016/j.epsl.2024.118796
Issue Date	2024-08-15
Doc URL	https://hdl.handle.net/2115/97465
Rights	©2024. This manuscript version is made available under the CC-BY-NC-ND 4.0 license http://creativecommons.org/licenses/by-nc-nd/4.0/
Rights(URL)	https://creativecommons.org/licenses/by-nc-nd/4.0/
Type	journal article
File Information	Heki_2024epsl_Husca.pdf

Hokkaido University Collection of Scholarly and Academic Papers : HUSCAP

Earth Planet. Sci. Lett., 640, 118796, 2024. doi:10.1016/j.epsl.2024.119896

Decoding multiple source signatures in coseismic ionospheric disturbances of the 2024 January M_w7.5 Noto-Peninsula earthquake, Central Japan

Kosuke Heki[1]

[1]*Dept. Earth Planet. Sci., Hokkaido Univ., N8 W10, Kita-ku, Sapporo-city, Hokkaido 060-0810, Japan*
email: heki@sci.hokudai.ac.jp

Highlights

1. Comprehensive study of coseismic ionospheric disturbance by the 2024 Jan. Noto-Peninsula earthquake
2. Multiple acoustic wave sources caused complicated waveforms and azimuthal dependences
3. Ionosphere recorded possible slow earthquake signals following the mainshock
4. Medium scale traveling ionospheric disturbance enhanced the coseismic signals

Abstract

Vertical crustal movements associated with large earthquakes excite various kinds of atmospheric waves. They propagate upward and often disturb ionosphere. Here, I report a case for the 2024 January 1 M_w7.5 earthquake that occurred in the northern tip of the Noto Peninsula, Central Japan, using a dense network of multi-GNSS receivers. A rectangular-shaped positive anomaly of ionospheric total electron content emerged ~9 minutes after the mainshock. The initial sharp peak was composed of two acoustic wave pulses excited at the two ends of the fault spanning ~100 km. It was followed by a series of smaller-amplitude broad peaks, the largest of which was possibly excited by a slow fault rupture near the NE edge of the fault ~8 minutes after the mainshock. These signatures become large where the wavefronts overlap with those of medium-scale traveling ionospheric disturbances, suggesting possible enhancement of the coseismic signals by downward displacements of high electron density regions in the ionosphere.

Keywords: 2024 Noto-Peninsula earthquake, GNSS-TEC, coseismic ionospheric disturbance, slow earthquake, MSTID

1. Introduction

A major seismic sequence has continued since 2020 around the northeastern (NE) tip of the Noto

Peninsula, Central Japan. Crustal deformation associated with this sequence suggests a shallow-angle tensile crack caused by the injection of non-volcanic fluid from lower crust (Nishimura et al., 2023). In this region, an M_w7.5 earthquake occurred at 7:10 UT (16:10 in JST), January 1, 2024. The rupture propagated bilaterally toward NE and SW from the epicenter along the fault spanning ~100 km.

The ruptured fault roughly overlaps the northern coast of the peninsula, and its NE tip reaches the middle point between the peninsula and the Sado Island (Fig.1a). The fault dips toward SE, and the faulting was reverse, with a small right-lateral component. It caused a rectangular-shaped region of crustal uplift of a meter or more along the northern coast of the peninsula (Fig.1b). Such deformation has been measured accurately using nationwide array of global navigation satellite system (GNSS) receivers in Japan called GNSS Earth Observation Network (GEONET) operated by Geospatial Information Authority (GSI) of Japan (Takamatsu et al., 2023).

GNSS can also be used for the measurements of total electron content (TEC), number of ionospheric electrons integrated along the line-of-sight (LoS), from the difference of phases of two microwave carriers. Large earthquakes excite atmospheric waves such as acoustic waves (AW) and internal gravity waves (IGW). They propagate upward and reach ionosphere and often cause coseismic ionospheric disturbances (CsID), which have been studied with GNSS for a few decades. The details of the GNSS-TEC technique and its applications for CsID studies are available in recent review articles such as Komjathy et al. (2016), Astafyeva (2019), and Heki (2021).

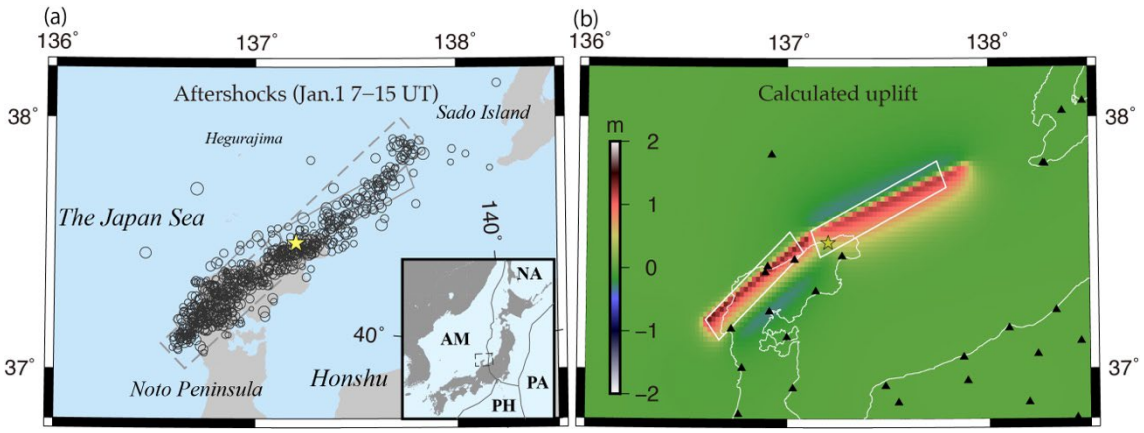

Fig.1. (a) Epicenter (yellow star) and aftershock distribution (circles) of the 2024 January 1 Noto-Peninsula earthquake by Japan Meteorological Agency (JMA, 2024). Surface projections of the faults by GSI (2004) and by NIED (2004) are indicated by solid and dashed lines, respectively. The inset map shows the tectonic setting of the region with the names of plates (AM: Amuria, NA: North America, PH: Philippine Sea, PA: Pacific). (b) Coseismic vertical crustal movements calculated using the January 2 version fault parameter by GSI (2024) assuming an elastic half space (Okada, 1992). Black triangles indicate positions of nearby GEONET GNSS stations. Uplift patterns based on later versions of fault models are given in Fig. S1.

Here I report comprehensive studies of CsID of this earthquake using TEC data from GEONET, emphasizing the benefit of a dense network for seismological studies. When earthquakes occurred over long faults, interference of AW pulses excited sequentially at different fault segments causes a complicated azimuthal dependence of the CsID waveform and amplitude, as clarified recently for the 2023 February M_w7.8 earthquake in southern Turkey (Bagiya et al., 2023). Here, I perform a more detailed study for this new case in Japan.

Heki et al. (2022) showed that GNSS-TEC can sense signatures of AW and IGW excited by slow fault slips like those in tsunami earthquakes. Here I look for small CsID signals that may originate from such slow fault ruptures. Finally, I will discuss interference between CsID and a phenomenon in the upper atmosphere, medium-scale traveling ionospheric disturbances (MSTID) that often emerge in winter daytime in the mid-latitude region (Otsuka et al., 2011).

2. Method and overview of CsID

2.1. CsID signals in multi-GNSS TEC time series

I use all the available GNSS data tracked by GEONET receivers, i.e., GPS, GLONASS, Galileo, and QZSS, using ~1300 stations uniformly distributed over the whole Japan (Fig.1b). Following Heki (2021), I converted the microwave carrier phase data into slant TEC (STEC). Fig.2 shows an example of STEC changes before and after the earthquake obtained by tracking eight GNSS satellites from a station 0319. The satellites include one quasi-zenith orbit satellite (J02), and the ionospheric piercing point (IPP) of its LoS, calculated assuming a thin ionosphere at 300 km height, show little movement relative to the ground. Other satellites have orbital periods of ~1/2 sidereal days, and IPP moves significantly during the period shown in Fig. 2.

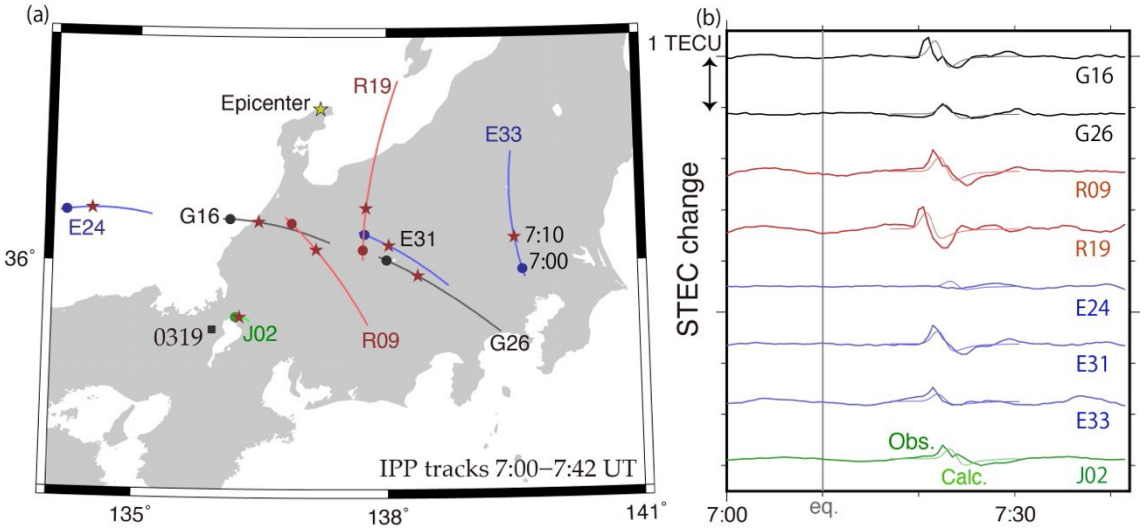

Fig.2. (a) Ground projections of IPP during 7:00-7:42 UT of 8 satellites viewed from the station 0319 located ~200 km SW of the epicenter. Dots and stars on the IPP tracks indicate those at 7:00 and the earthquake occurrence time (7:10), respectively. GPS (G16, G26), GLONASS (R09,

R19), Galileo (E24, E31, E33), and QZSS (J02) satellites are shown with black, red, blue, and green colors, respectively. (b) STEC residual time series obtained by fitting degree-5 polynomials to the original time series. A typical N-shaped pulse emerge around 10 minutes after the earthquake, but their arrival times, amplitudes and waveforms are not uniform ("Obs.", thick curves). They are compared with numerically synthesized STEC changes ("Calc.", thin curves) assuming N-shaped pulse with a period of 160 seconds propagataing as AW from the epicenter, a yellow star in (a). "Calc" time series are meaningful only in a relative sense, and an arbitrary scale factor is given for the whole.

In Fig. 2b, we see typical N-shaped signatures made by AW propagated from the uplift area (Fig.1b) to the ionospheric F region taking about 10 minutes. The amplitude of R19-0319 pair is ~0.43 TECU (1 TEC unit, TECU, means 10^{16} electrons/m^2), and its ratio to the background vertical TEC (Fig. S2) is consistent with the empirical law based on past examples shown in Fig. S3. Fig.2b compares observed TEC changes with those numerically synthesized in the same way as in Heki and Fujimoto (2022) and Kundu et al. (2021). I first let a single N-shaped AW pulse, from the epicenter, propagate upward in an atmosphere with a known velocity structure (US Standard Atmosphere 1976). Then, I integrated the electron density along LoS to calculate perturbation in STEC. There, in addition to the distance from the AW source, two factors, geomagnetism and LoS geometry with the AW wavefront, influence relative amplitudes and arrival times (Fig.S4).

Fig. 2b shows that the observed relative amplitudes and arrival times are well reproduced by numerical simulations. On the other hands, some features are not well reproduced in this single-source simulation. For example, for the G16-0319 pair, the observed main pulse is composed of a large pulse and a smaller sub-pulse arriving ~1 minute later. However, the synthesized curve shows one peak in the middle of the two observed peaks. Similar signatures are visible in satellites whose IPP are located at the SW of the epicenter, e.g., R09, and J02, but are not clear in satellites located at the SE of the epicenter, e.g., R09, E31, and E33. This will be discussed later in Section 3.2. For satellites such as G16 and R19, the main peaks are followed by multiple smaller amplitude peaks over the subsequent ~15 minutes. They are not reproduced by the single-source numerical simulations. Their origins will be discussed in Section 3.3.

2.2. Propagation of CsID

Next, I convert STEC to vertical TEC (VTEC) by first removing the inter-frequency bias and secondly by multiplying the de-biased STEC by the cosine of the incident angle of LoS to the hypothetical thin ionosphere at 300 km altitude. I inferred the biases so that the de-biased VTEC align with those from global ionospheric map (GIM) from CDDIS (cddis.nasa.gov). VTEC shows simpler temporal variation than STEC and can be fit with polynomials with smaller degrees. Fig.3 shows eight snapshots of VTEC anomalies, residuals from degree-3 polynomials for period 6.5-8.0 UT. Here, because the satellite (J02) has a quasi-zenith orbit, the ground projections of IPP remain close to the

GNSS receivers. We can see elongated shape positive TEC anomaly emerged at 7:20 and propagated southward with the wavefront getting more circular as it propagates.

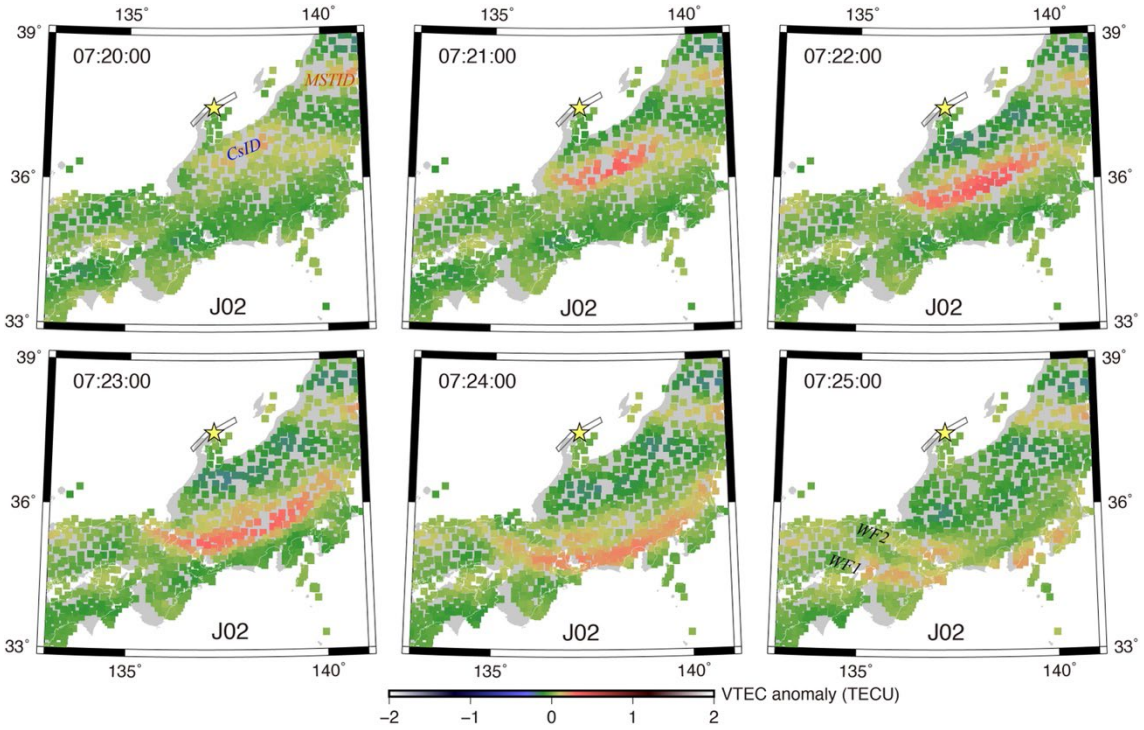

Fig.3. Distribution of VTEC residuals of J02 plotted on map every minute from 07:20 to 07:25. A rectangular shaped positive anomaly emerges at 07:20. Another belt of positive anomalies running east-west at latitude ~38N is a wavefront of MSTID. The CsID wavefront becomes rounder as it propagates, and splits into two (WF1 and WF2 shown in the 07:25 panel). Similar residual VTEC maps drawn using other GNSS satellites are given in Fig. S5.

The wavefront seems to split into two after 07:24 as indicated with labels WF1 and WF2. WF2 corresponds to small sub-peaks that lags in time by ~1 minutes in the J02 STEC time series in Fig.2b. In addition to CsID signatures, we can see another wavefront running east-west at latitude ~38N. This is one of the daytime MSTID wavefronts that typically appear in winter (Otsuka et al., 2011). It propagates by ~0.2 km/s as IGW. This is much slower than CsID, but one can recognize its southward propagation by carefully comparing its position at different epochs. The interaction of MSTID with CsID will be discussed in Section 3.4.

The propagation speeds of these CsID can be inferred from time-distance plots shown in Fig.4 using three different satellites G16, R19, and E24. They all show strong anomaly emerges ~9 minutes after the earthquake above the epicenter and propagate by the speed of sound wave in the ionospheric F region (the best-fit line has a slope of 0.89 km/s). On the other hand, we do not see components propagating with the speed of Rayleigh wave (3.5-4.0 km/s) or IGW (0.2-0.3 km/s).

In addition to the initial anomaly, we can see, in all the three satellites, many smaller peaks follow

the main one over the subsequent ~15 minutes with the same speed. Here I call them "later peaks". I assumed the propagation speed of 0.89 km and converted the TEC anomaly time series back to those above the epicenter. I then averaged all the station data to get "stacked anomaly" shown in Fig. 4b1-b3. The average of the three stacked time series is given in Fig. 4c, where I name the peaks as A, A', B1, B2, C1, C2, and C3. A and A' correspond to the two wavefronts seen in the 7:25 panel of Fig. 3 (WF1, WF2). B2 is the strongest of the later peaks, and I discuss its origin in Section 3.3.

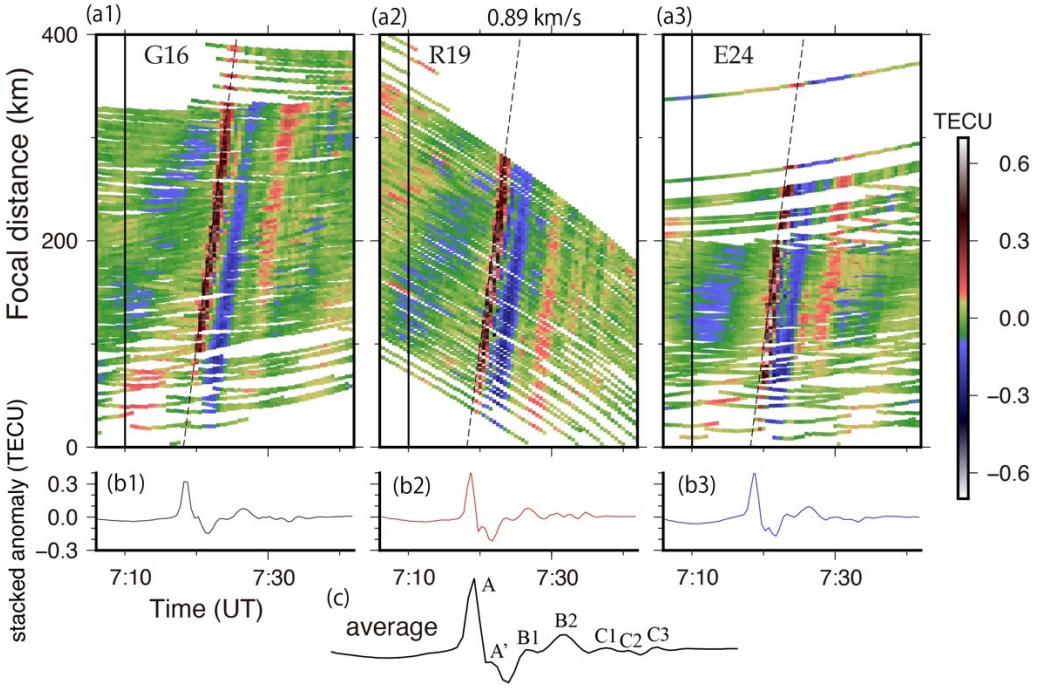

Fig.4. (a) Focal distance (vertical axis) – time (horizontal axis) plots of the VTEC anomalies by G16 (left), R19 (middle), and E24 (right) satellites. Here I isolated components propagating southward, by limiting the azimuth of IPP viewed from the epicenter within the range 150-210 degrees from the north. (b) By assuming the propagation speed of 0.89 km/s, I let them back-propagate to the epicenter, and obtained the average of all the data to get the stacked anomaly for the three satellites. (c) I named the main (A, A') and later (B1, B2, C1, C2, C3) peaks, and indicated them to the average waveform of the three satellites.

3. Discussions

3.1. Shape of the initial anomaly

A rectangular shaped positive TEC anomaly, reflecting the fault shape, emerged ~9 minutes after the mainshock (Fig.5). This initial anomaly is hardly visible with J02 satellite (Fig. 3) because the LoS toward the zenith would penetrate both the positive and negative electron density anomalies that cancel each other (see Fig. 1 of Heki, 2024). The LoS to satellite E24, on the other hand, penetrates the wavefront in a shallow angle. Hence, it first penetrates the upper positive electron density anomaly region and senses the initial signature of CsID.

Fig. 5b catches the initial shape of the anomaly reflecting the uplift area extending NE-SW by ~100 km. The wavefront preserves the rectangular shape for a few minutes but becomes circular as it propagates hundreds of kilometers outward. As discussed in the next section, seismological studies by National Research Institute for Earth Science and Disaster Resilience (NIED, 2024) suggest that the amount of uplift is larger near the NE and SW tips of the fault. However, Fig.5b seems to show larger anomalies just above the epicenter rather than above the two ends. This may be due to a time lag in uplift between the central segment and the two ends. The rupture started at the center, and it took ~0.5 minute for the rupture to arrive at the SW end and somewhat later at the NE end.

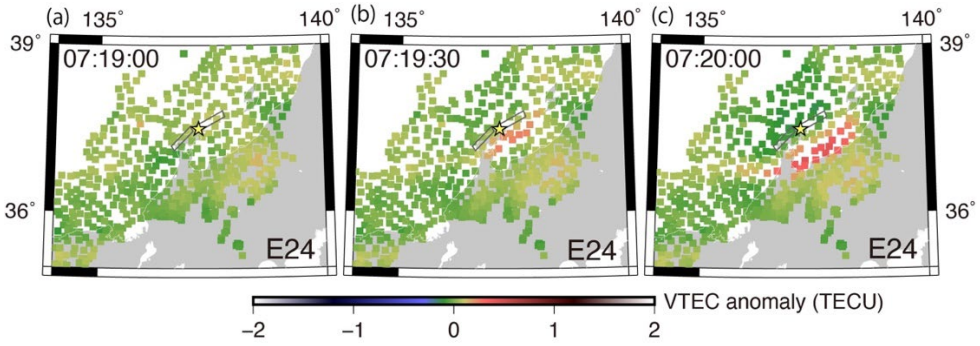

Fig.5. The VTEC anomaly caught by the E24 satellite when it first emerged at 07:19:30, ~9 minutes after the earthquake. The shape of the positive anomaly with NE-SW elongation resembles to the uplift area shown in Fig.1b.

3.2. Two sources in the main shock

The main perturbation is accompanied by a small sub-peak (peak A and A' in Fig. 4c). Fig. 2b suggests that the sub-peak A' was visible only with satellites whose IPP is located to the SW of the epicenter. Here, I show that such azimuthal dependence could occur due to interference of two AW pulses excited at two points on the fault. I follow Bagiya et al. (2023), who successfully explained similar azimuthal dependence of the 2023 Turkey earthquake CsID.

In the 2024 Noto-Peninsula earthquake, the rupture started at the middle of the fault, elongated NE-SW, and propagated toward the two ends (NIED, 2024). The rupture sequence inferred from seismic records shows that coseismic slip remained ~1 m or so near the epicenter while slips reached a few meters near the NE and SW ends of the fault, separated ~100 km. Disaster Prevention Research Institute, Kyoto University, by using seismometer arrays in Japan, further inferred that the rupture of the NE segment was ~13 seconds later than the SW one (DPRI, 2024).

Fig.2b shows that the observed CsID can be reproduced, to some extent, by assuming a single AW source at the epicenter. However, the observed signals would be better reproduced by assuming two AW pulses generated at two points shifted NE and SW from the epicenter. Their interference may explain the diversity of amplitudes and waveforms at stations in various azimuths from the source.

Fig. 6 compares the CsID waveforms with the satellite R19 at seven stations. Their IPP ground projections at 7:20 (approximate time of CsID occurrence) are all located at distance ~150 km but in different azimuths from the epicenter. As suggested in Section 2.1, CsID observed from SW of the epicenter show distinct two peaks (A and A' at 0392, Fig. 6b). Arrival times of A and A' get closer as the IPP moves counterclockwise, and the two peaks merge making single strong peaks for IPP at the SE side of the epicenter (e.g., at 0338, 1007). The amplitude decays as IPP moves further counterclockwise (e.g., at 0298).

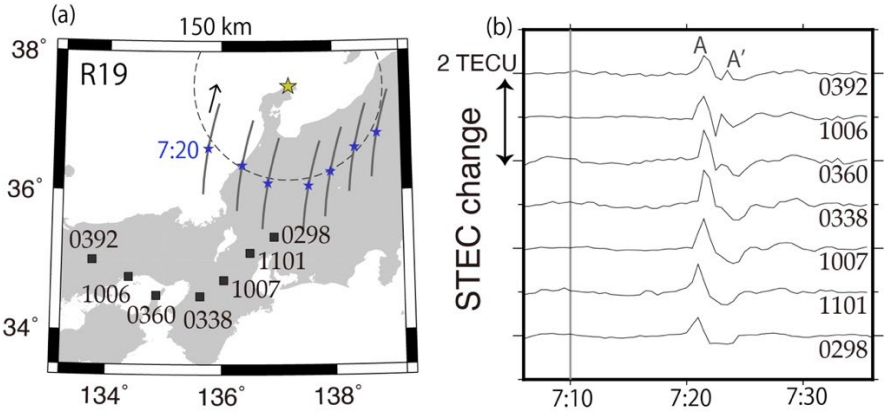

Fig.6. (a) Seven stations (black squares) whose IPP of R19 satellite at 7:20 (blue stars) are ~150 km away from the epicenter. (b) Comparison of CsID waveforms at these stations observed with R19. The STEC time series at 0392 and 1006 show two clear peaks marked as A and A'. They merge as the IPP goes counterclockwise and become one large peak at 0338, 1007, and 1101.

Fig. 7 compares results of numerical simulation of CsID assuming one AW source at the epicenter (Fig.7b) and two sources separated 100 km (Fig.7c), synthesized in the same way as "Calc" curves in Fig. 2b. In the two-sources case, the total signals (Fig.7d) are composed of two peaks or one strong peak at IPPs located in SW (P1, P2) and SE (P4, P5), respectively, reproducing the general pattern in Fig. 6b. I here assume the two sources interact linearly. This suggests that the azimuthal asymmetry of the main disturbance is due to the interference of two AW pulses.

Here, I assume that the AW sources#1 and #2 have the same strengths and occurrence times. I assume somewhat shorter period for sources #1 and #2 (120 seconds) than source #0 (160 seconds) considering the difference in AW source areas. DPRI (2024) suggested that the slip at the NE segment occurred ~13 seconds later than the SW one, although their seismic moments are similar. In fact, it may be too simple to assume only two AW sources considering that smaller AW pulses would have been generated continuously along the entire fault. By increasing the number of AW sources and further tuning their intensities, the resemblance may improve. This is, however, beyond the scope of the current study. Here I just demonstrate that the pattern seen in Fig. 6 can be reproduced with a simple model assuming only two AW sources.

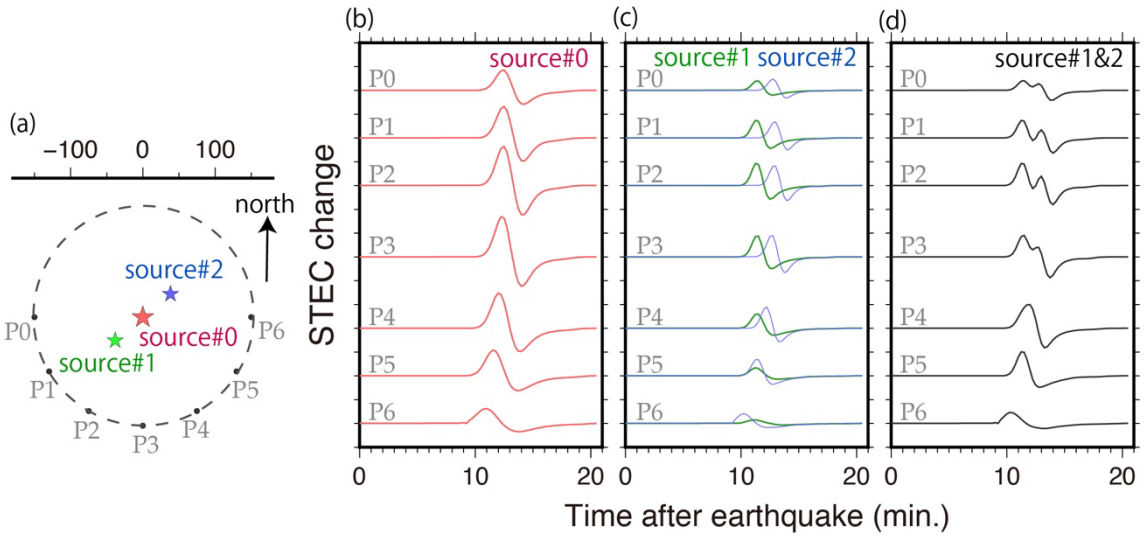

Fig.7. STEC anomaly time series numerically synthesized at seven IPPs (P0-P6) 150 km from the epicenter (a) are compared in (b). The unit of the vertical axis is arbitrary, and the amplitudes are meaningful only in relative sense. For the single source case (b), amplitudes of CsID reflect two factors, geomagnetic field, and geometry of LoS with the wavefront (Fig. S5). If we replace this "source #0" with two sources of equal strength, separated 100 km in NE-SW (sources #1 and #2), individual AW signatures have different amplitude and time lags at points in different azimuths from the epicenter (c). Their sum (d) has distinct two peaks at P0 but the two peaks merge at P5 resulting in one strong peak. Here I assumed the LoS geometry of the R19 satellite. The period of the N-shaped pulse is assumed as 160 seconds for (b) and 120 seconds for (c) and (d).

3.3. Origin of the later peaks: Possible slow fault slips 5-8 minutes after the mainshock

The main perturbation (A and A' discussed in the previous section) is followed by a series of small peaks, named as B1, B2, C1, C2, C3 (Fig.4c), occurring sequentially over a period of ~15 minutes. They have relatively broad peaks and chase the main perturbation with the same AW speed of ~0.9 km/s (Fig.4a). The largest of these later peaks, B2, has an amplitude of ~0.08 TECU and appeared ~8 minutes after the main shock signature. What caused these small peaks?

According to JMA (2024), the largest aftershock (M_{JMA}6.1) occurred at 7:18 (~8 minutes after the mainshock) near the SW end of the fault. First, I examine the relevance of the peak B2 to this aftershock. The smallest earthquake whose CsID has been detected in Japan is the 2007 M_w6.6 Chuetsu-oki earthquake (Cahyadi and Heki, 2015). The magnitude of this largest aftershock is even smaller, and the scaling law (Fig.S3) could hardly predict its CsID amplitude. However, such a small earthquake may still make a detectable CsID considering that Maletckii et. al. (2023) found CsID for earthquakes with magnitudes down to 5.5.

Fig. 8a compares the stacked waveform obtained by GNSS stations in various bins of the azimuths of their IPP from the epicenter. If the coordinate of the AW source is correctly assumed, the occurrence

times of the anomaly would not depend on azimuths. This is the case for the initial peak (A). However, the B1 and B2 peak occurrence times systematic change for different azimuths, i.e., they occur earlier when viewed from the east and later from the west. If their origins are somewhere within the aftershock region, they need be located to the NE of the epicenter. Fig. 8b shows that the occurrence times become nearly uniform by assuming a new coordinate for their origin near the NE end of the fault (Fig.8c).

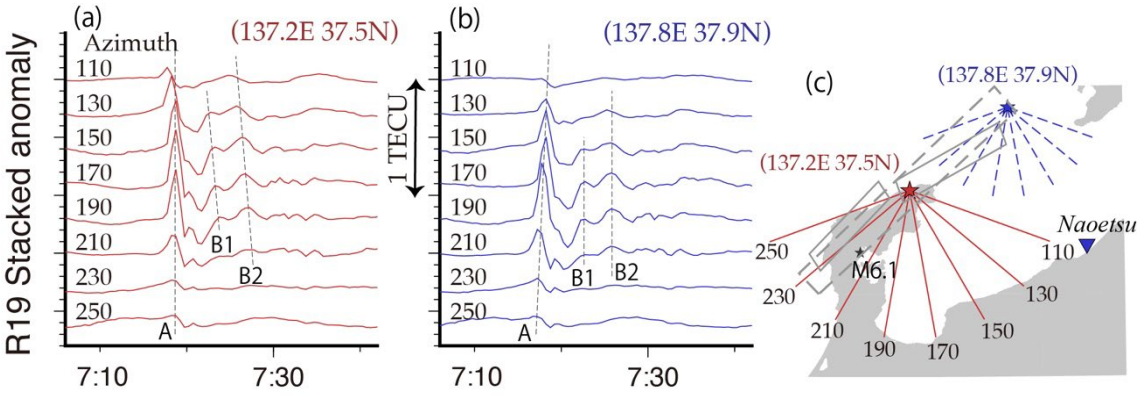

Fig.8. VTEC anomalies with the R19 satellite stacked in the same way as Fig.4b. In doing so, I classified the data with the azimuth of IPP from the assumed epicenter into 20 degree bins (e.g., "110" bin includes data with azimuths 110 ± 10 degrees). We used the epicenter of the mainshock in (a) and a hypothetical epicenter at the NE edge of the fault in (b). The occurrence times of B1 and B2 in (a) systematically change for different azimuths, suggesting that the assumed position (red star) is wrong. Simultaneous occurrences of B1 and B2 in (b), on the other hand, suggest they propagated from the blue star in (c). A black star in (c) indicates the epicenter of the largest aftershock that occurred ~8 minutes after the mainshock. Red and blue lines in (c) shows azimuthal bins used in (a) and (b), respectively. Blue triangle in (c) shows the position of the Naoetsu wave gauge.

This new position is far from the epicenter of the largest aftershock located SW of the mainshock epicenter (Fig.8c). In fact, by assuming a source at the M6.1 aftershock epicenter, azimuthal dependence of their occurrence times becomes worse. Thus, I think it unlikely that B2, the largest of the later peaks, was caused by this largest aftershock (i.e., this aftershock was not large enough to cause a detectable CsID). The second largest later peak B1 that occurred ~5 minutes after the mainshock would also have been excited near the NE end of the fault (no large aftershocks are reported there, either). Regarding the small peaks C1, C2, and C3, their occurrence times appear more uniform in azimuthal bins in Fig. 8a than in Fig. 8b. Therefore, the source of these signals would be somewhere else.

The absence of corresponding seismic records suggests that the AW responsible for the B1 and B2 peaks were generated by slow fault slips whose rupture took one minute or more. In fact, Fujii and

Satake (2024) reports an unexplained large tsunami height at the Naoetsu wave gauge (Fig. 8c), which may support the occurrence of a tsunami earthquake shortly after the mainshock. An M_w6 rupture would normally end within 10 seconds. If the rupture was ten times as slow, it may generate little seismic waves. It, however, may generate significant AW and CsID with a period of a few minutes (Heki et al., 2022). Fluid injection is thought responsible for the series of seismic activity in the northern Noto-Peninsula since 2020 (Nishimura et al., 2023). Gugliemi et al. (2015) suggested that fluid injection into a fault surface with non-uniform friction property may induce aseismic slips. Possible occurrence of slow slips large enough to cause visible CsID may be related to this fluid injection.

3.4. Interaction between CsID and MSTID

About 9 hours before the 2024 January 1 Noto-Peninsula earthquake, an X5.0 class solar flare occurred (swc.nict.go.jp). However, indices suggest that geomagnetic activity is not yet so high at the time of the earthquake (Fig. S6). Daytime MSTIDs frequently occur in the Japanese Islands during winter. Such daytime MSTIDs have wavefronts running east-west and propagate southward with the IGW speed (Otsuka et al., 2011).

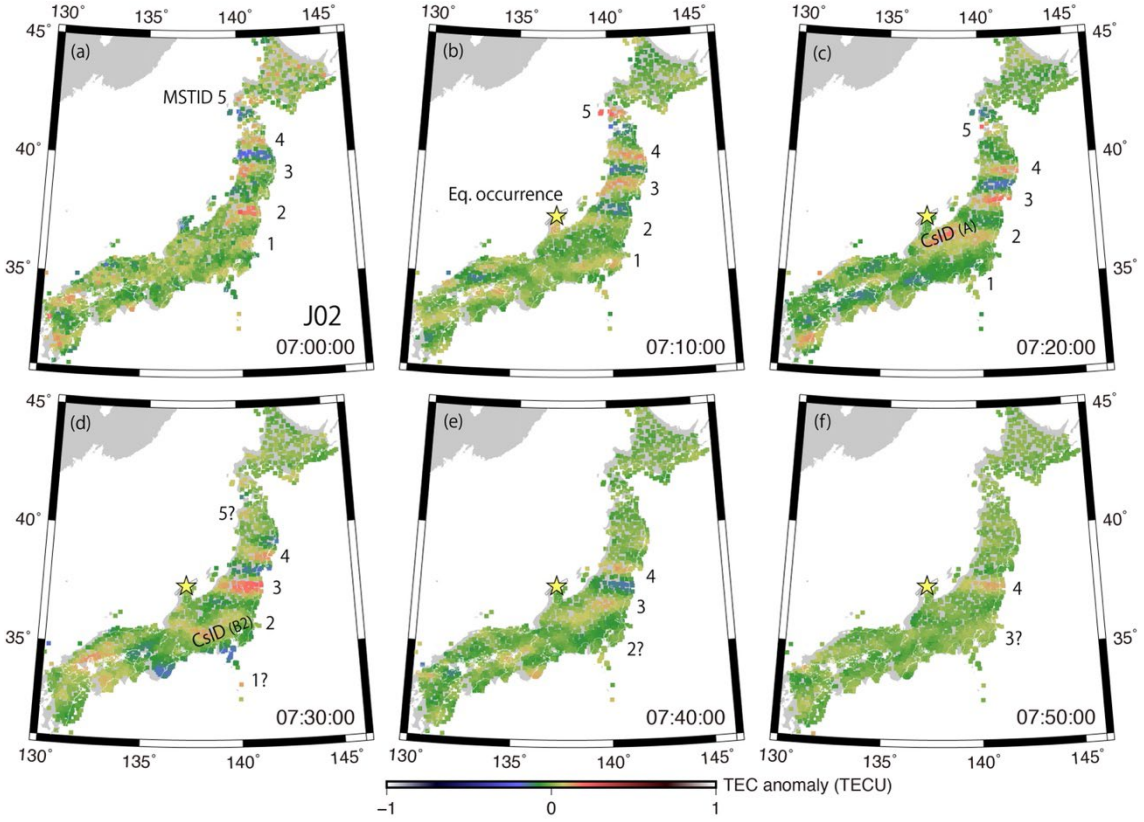

Fig.9. Six snapshots of the VTEC anomalies with J02 satellite. Here the same data set as Fig. 3 is shown in larger spatial and temporal windows. Here, we can see slower (~0.2 km/s) southward propagation of five MSTID wavefronts together with faster (~0.9 km/s) outward propagation of

two CsID wavefronts. Occasional overlap of CsID signals of the main peak (A) and the largest later peak (B2) with MSTID wavefront #2 may have enhanced the CsID signals (Fig. 10).

Around the occurrence time of the Noto-Peninsula earthquake, I found multiple wavefronts of such MSTID propagate from north to south across the Japanese Islands. Fig. 9 shows VTEC anomalies 7:00-7:50 viewed with the J02 satellite. There, we can see five wavefronts moving as fast as ~0.2 km/s southward. We give serial numbers 1-5, from south to north, to these wavefronts. They are not always clear throughout the period but are easily identified in the six panels of Fig. 9.

The initial CsID peak (peak A in Fig. 4c) overlaps with MSTID wavefront #2 (Fig.9c). Because CsID propagates faster, it soon overtook MSTID. About 10 minutes later, the largest later peak of CsID (peak B2 in Fig. 4c) caught up with MSTID 2 (Fig. 9d). After moving together for a few minutes, the CsID wavefront again overtook MSTID. Here I examine if these CsID and MSTID had interactions.

Fig. 10 shows the distance-time plot of CsID drawn using the J02 satellite. I selected this satellite because it stays near zenith and keeps the geometry of LoS with the MSTID and CsID wavefronts nearly stationary during this period (Fig.2a). This makes the J02 satellite suitable for discussing the change of observed disturbance amplitudes. Fig. 10 shows the data whose IPP are in the azimuth range between 120 and 240 degrees as viewed from the epicenter. Then, both southward moving MSTID and outward moving CsID make linear feature in this plot (red colors in Fig 10a).

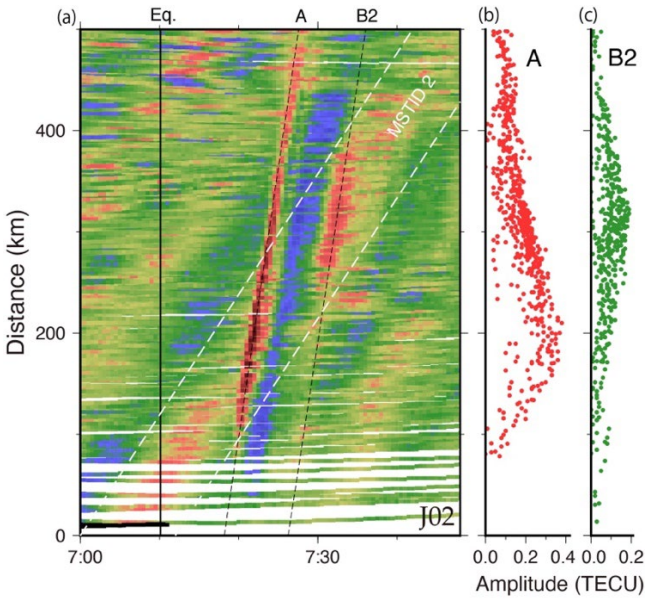

Fig.10. (a) Distance-time plot of the VTEC anomalies obtained using the J02 satellites staying near zenith. I selected data whose IPPs are within the azimuth range 120-240 degrees from the epicenter. I used the same color palette as in Fig.4a. MSTID signatures, within the two dashed lines, are seen to propagate by ~0.2 km/s. Amplitudes of the CsID, A and B2, are given in (b) and (c), respectively, as a function of the focal distance. Here, we see the CsID amplitudes are

enhanced where they overlap the MSTID wavefront #2 in Fig. 9.

There we notice that CsID signal amplitudes are larger where they overlap the MSTID wavefront. In fact, the B2 signal is visible only where it overlaps the MSTID. It should be noted that I use a satellite that remains around zenith and the changes in amplitudes do not reflect changes in LoS geometry. Otsuka et al. (2013) suggested that peak electron density heights are displaced tens of kilometers downward where MSTID makes positive TEC anomalies. CsID, driven by AW from the ground, would decay as it propagates upward. Hence, downward shift of the peak electron density would amplify the CsID signals. This may also have facilitated the detection of small CsID signals in a series of later peaks that may not be visible under normal conditions.

3.5. Preseismic TEC changes

Last, I discuss if the observed TEC shows any changes prior to the mainshock of the Noto-Peninsula earthquake as found before the 2011 Tohoku-oki earthquake (Heki, 2011). Heki (2021) and Heki et al. (2024) compiled the changes in TEC trend immediately before earthquakes of ~20 past large earthquakes and found that the leading time and the intensity of the anomaly (relative to the background) scale with the fault length and fault areas, respectively. According to these scaling laws, the anomaly of an M_w7.5 earthquake is expected to start ~12 minutes before the earthquake and to grow as large as ~0.7 % of the background VTEC.

For the Noto-Peninsula, this means that the trend change starts shortly before 7 UT and that its intensity at the time of the earthquake would be around 0.12 TECU. As shown in Fig. 9, the daytime MSTIDs, having larger amplitudes, propagate southward during this period. Hence, I think it difficult to detect small precursory TEC changes, even if they occurred, in a convincing way.

4. Conclusions

I conclude this study as follows,

(1) The 2024 January 1 Noto-Peninsula earthquake left clear coseismic disturbance of ionosphere, and they were observed using the dense GNSS network in Japan.

(2) The shape of the TEC anomaly preserved that of the uplifted region when it initially emerged above the fault.

(3) The main peak had azimuth-dependent amplitudes and waveforms originating from the interference of the two distinct AW sources.

(4) The main phase was followed by numbers of smaller peaks, and the largest one was possibly excited ~8 minutes after the mainshock by a slow earthquake around the NE edge of the fault.

(5) MSTID may have amplified the coseismic disturbance signals.

Acknowledgements. I thank two anonymous referees for constructive reviews. The GNSS raw data

files are downloaded from Geospatial Authority of Japan (terras.gsi.go.jp). Data downloaded from public domain data base include global ionospheric map (cddis.nasa.gov), space weather data (omniweb.nasa.gov, swc.nict.go.jp). Aftershock data are obtained from Japan Meteorological Agency (www.data.jma.go.jp/svd/eqev/data/daily_map/).

Competing interests. The author declares that he has no known competing financial interests or personal relationships that could have appeared to influence the work reported in this paper.

References

Astafyeva, E., 2019. Ionospheric detection of natural hazards. Rev. Geophys. 57(4), 1265–1288, doi:10.1029/2019RG000668

Bagiya, M. S., Heki, K., Gahalaut, V. K., 2023. Anisotropy of the near-field coseismic ionospheric perturbation amplitudes reflecting the source process: The 2023 February Turkey earthquakes. Geophys. Res. Lett. 54, e2023GL103931, doi:10.1029/2023GL103931.

Cahyadi, M.N., Heki, K., 2015. Coseismic ionospheric disturbance of the large strike-slip earthquakes in North Sumatra in 2012: M_w dependence of the disturbance amplitudes. Geophys. J. Int. 200, 116-129.

DPRI Kyoto Univ., 2024, https://sms.dpri.kyoto-u.ac.jp/topics/2024noto_source_20240115.pdf

Fujii, Y., Satake, K., 2024. Slip distribution of the 2024 Noto Peninsula earthquake (M_{JMA} 7.6) estimated from tsunami waveforms and GNSS data. Earth Planets Space 76, 44, doi:10.1186/s40623-024-01991-z.

GSI, 2024, https://www.gsi.go.jp/cais/topic20240101Noto.html

Guglielmi, Y., Cappa, F., Avouac, J.-P., Henry, P., Elsworth, D., 2015. Seismicity triggered by fluid injection-induced aseismic slip. Science 348, 1224-1225, doi:10.1126/science.aab0476.

Heki, K., 2011. Ionospheric electron enhancement preceding the 2011 Tohoku-Oki earthquake. Geophys. Res. Lett. 38, L17312, doi:10.1029/2011GL047908.

Heki, K., 2021. Chapter 21: Ionospheric Disturbances Related to Earthquakes in Ionospheric Dynamics and Applications, Geophys. Monograph 260, edited by C. Huang, G. Lu, Y. Zhang, and L. J. Paxton, pp.511-526, Wiley/American Geophysical Union, ISBN:978-1-119-50755-0, doi:10.1002/9781119815617.ch21.

Heki, K., 2024. Atmospheric resonant oscillations by the 2022 January 15 eruption of the Hunga-Tonga Hunga-Ha'apai volcano from GNSS-TEC observations. Geophys. J. Int. 236, 1840-1847, doi:10.1093/gji/ggae023.

Heki, K., Fujimoto, T., 2022. Atmospheric modes excited by the 2021 August eruption of the Fukutoku-Okanoba volcano, Izu-Bonin Arc, observed as harmonic TEC oscillations by QZSS. Earth Planets Space 74, 27, doi:10.1186/s40623-022-01587-5.

Heki, K., Bagiya, M.S., Takasaka, Y., 2022. Slow fault slip signatures in coseismic ionospheric disturbances. Geophys. Res. Lett. 49, e2022GL101064, doi:10.1029/2022GL101064.

Heki, K., Nakatani, M., Zhan, W., 2024. Ionospheric changes immediately before the 2008 Wenchuan earthquake. Adv. Space Res., doi:10.1016/j.asr.2024.02.011.

JMA, 2024, www.data.jma.go.jp/svd/eqev/data/daily_map/

Komjathy, A., Yang, Y.-M., Meng, X., Verkhoglyadova, O., Mannucci, A. J., Langley, R. B., 2016. Review and perspectives: Understanding natural-hazards-generated ionospheric perturbations using GPS measurements and coupled modeling. Radio Science 51, 951–961. doi:10.1002/2015RS005910

Kundu, B., Senapati, B., Matsushita, A., Heki K., 2021. Atmospheric wave energy of the 2020 August 4 explosion in Beirut, Lebanon, from ionospheric disturbances. Sci. Rep. 11, 2793, doi:10.1038/s41598-021-82355-5.

Maletckii, B., Astafyeva, E., Sanchez, S. A., Kherani, E. A., de Paula, E. R., 2023. The 6 February 2023 Türkiye earthquake sequence as detected in the ionosphere. J. Geophys. Res. Space Phys. 128, e2023JA031663. doi:10.1029/2023JA031663

NIED, 2024, www.kyoshin.bosai.go.jp/kyoshin/topics/noto_20240101/inversion/inv_index.html

Nishimura, T., Hiramatsu, Y., Ohta, Y., 2023. Episodic transient deformation revealed by the analysis of multiple GNSS networks in the Noto Peninsula, central Japan. Sci. Rep. 13, 8381, doi:10.1038/s41598-023-35459-z.

Okada, Y., 1992. Internal deformation due to shear and tensile faults in a half-space. Bull. Seismol. Soc. Am. 82, 1018–1040.

Otsuka, Y., Kotake, N., Shiokawa, K., Ogawa, T., Tsugawa, T., Saito, A., 2011. Statistical study of medium-scale traveling ionospheric disturbances observed with a GPS receiver network in Japan. Chapter 21 pp. 291-299, in M.A. Abdu, D. Pancheva (eds.), A. Bhattacharyya (Coed.), Aeronomy of the Earth's Atmosphere and Ionosphere, IAGA Special Sopron Book Series 2, Springer, doi:10.1007/978-94-007-0326-1_21.

Otsuka, Y., Suzuki, K., Nakagawa, S., Nishioka, M., Shiokawa, K., Tsugawa, T., 2013. GPS observations of medium-scale traveling ionospheric disturbances over Europe. Ann. Geophys. 31, 163-172, doi:10.5194/angeo-31-163-2013.

Takamatsu, N., Muramatsu, H., Abe, S., Hatanaka, Y., Furuya, T., Kakiage, Y., Ohashi, K., Kato, C., Ohno, K., Kawamoto, S., 2023. New GEONET analysis strategy at GSI: daily coordinates of over 1300 GNSS CORS in Japan throughout the last quarter century. Earth Planets Space 75, 49, doi: 10.1186/s40623-023-01787-7

Supplementary materials

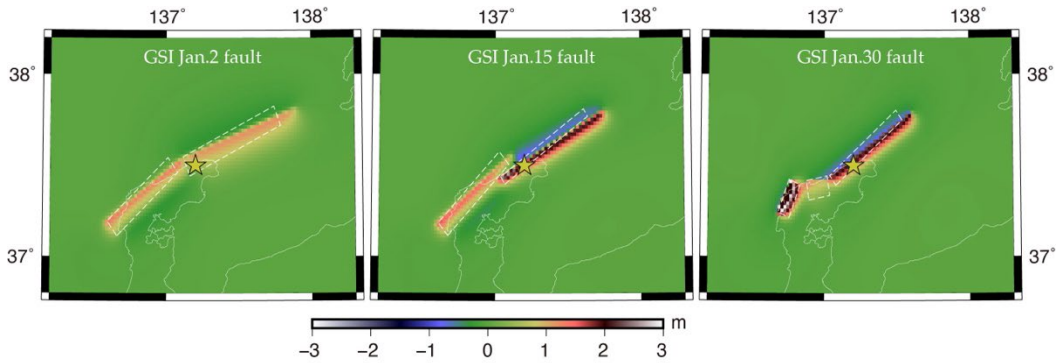

Fig. S1. Comparison of the distribution of coseismic surface uplift with the three different versions of the rectangular fault models published by GSI (2024) assuming an elastic half space (Okada, 1992). Because they are based on crustal deformation measured on land by GNSS and interferometric synthetic aperture radar (InSAR), resolution is not good for the submarine part of the fault.

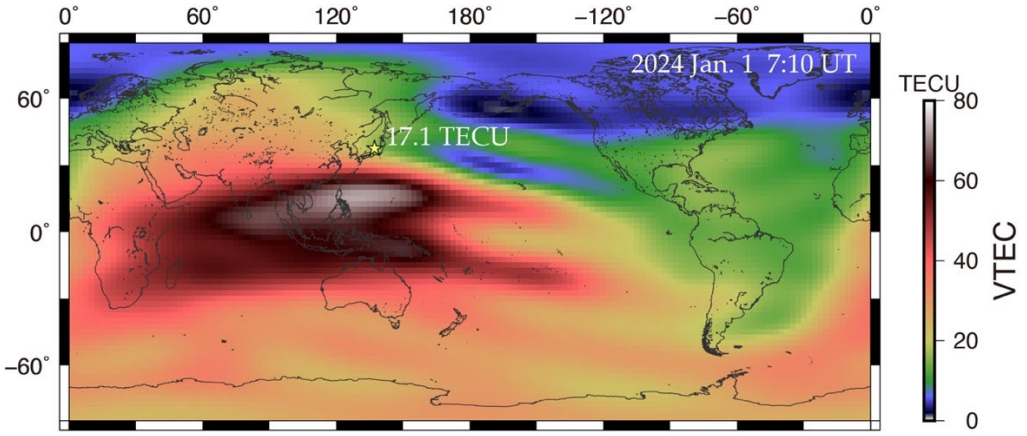

Fig. S2. Global ionospheric map (GIM) at the time of the mainshock obtained from CDDIS (cddis.nasa.gov). The background VTEC at the epicenter was ~17.1 TECU.

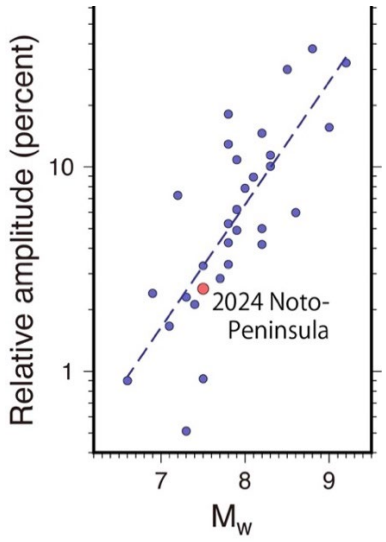

Fig. S3. Amplitude of CsID relative to the background VTEC in percent (vertical axis) versus moment magnitude (M_w) of the earthquakes compiled in Heki et al. (2022). For the 2024 Jan. 1 Noto-Peninsula earthquake (M_w7.5), the pair R19-0319 showed the amplitude of ~0.43 TECU (Fig.2), which is ~2.5 % of the background VTEC (Fig. S2). This new case, shown with red, fit well with past cases.

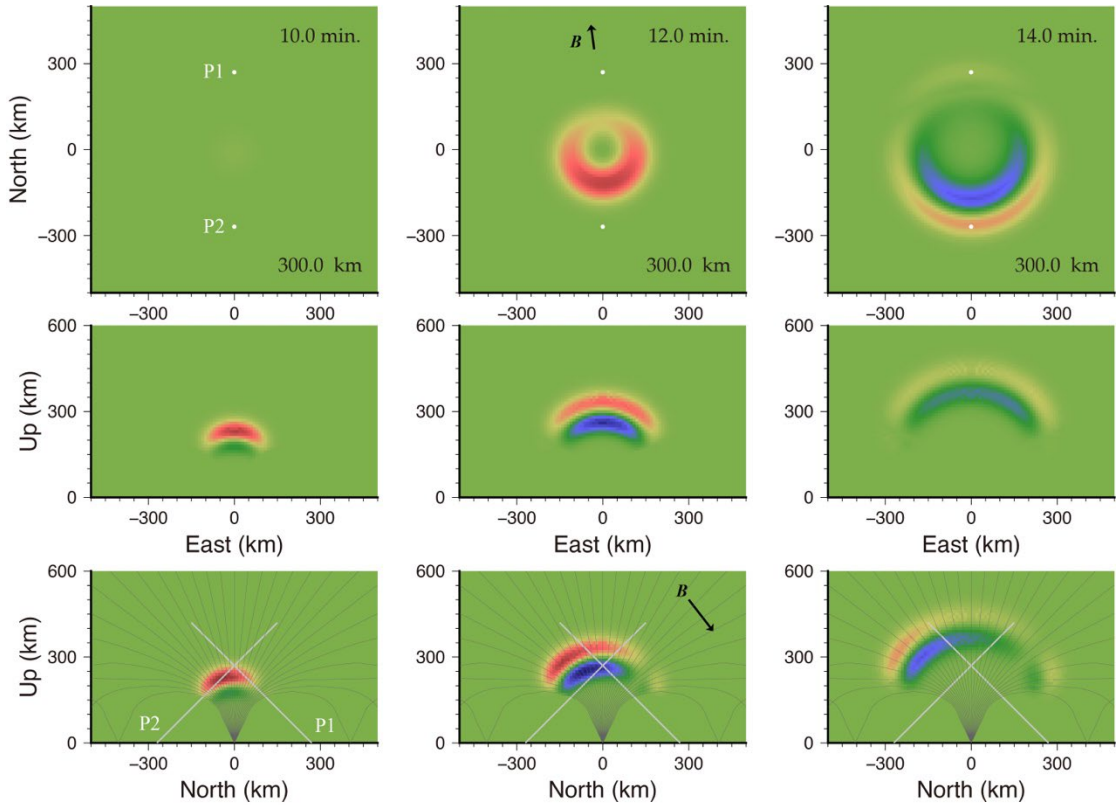

Fig. S4. Three-dimensional structure of positive (red) and negative (blue) electron density anomalies by a numerical simulation of upward propagation of an AW pulse with a period of 160 seconds in a realistic atmosphere (US Standard Atmosphere 1976). They are snapshots at three time epochs, 10 (left), 12 (middle), and 14 minutes (right) after earthquake. They are shown as plan view (top), east-west profile (middle), and north-south profile (bottom). The intensity of the electron density anomalies is meaningful only in a relative sense and does not have a unit. Ionospheric electrons in the F region can move only along the geomagnetic field, which causes southward beam of the CsID. I assumed the geomagnetic field direction above the 2024 Noto-Peninsula earthquake epicenter (vectors shown as ***B***). I compare two LoS, from P1 and P2 located to the north and south of the epicenter, respectively. The LoS from P1 penetrates both positive and negative electron density anomalies and show small changes in STEC. On the other hand, LoS from P2 first penetrates positive and then negative parts, resulting in clear N-shaped TEC changes.

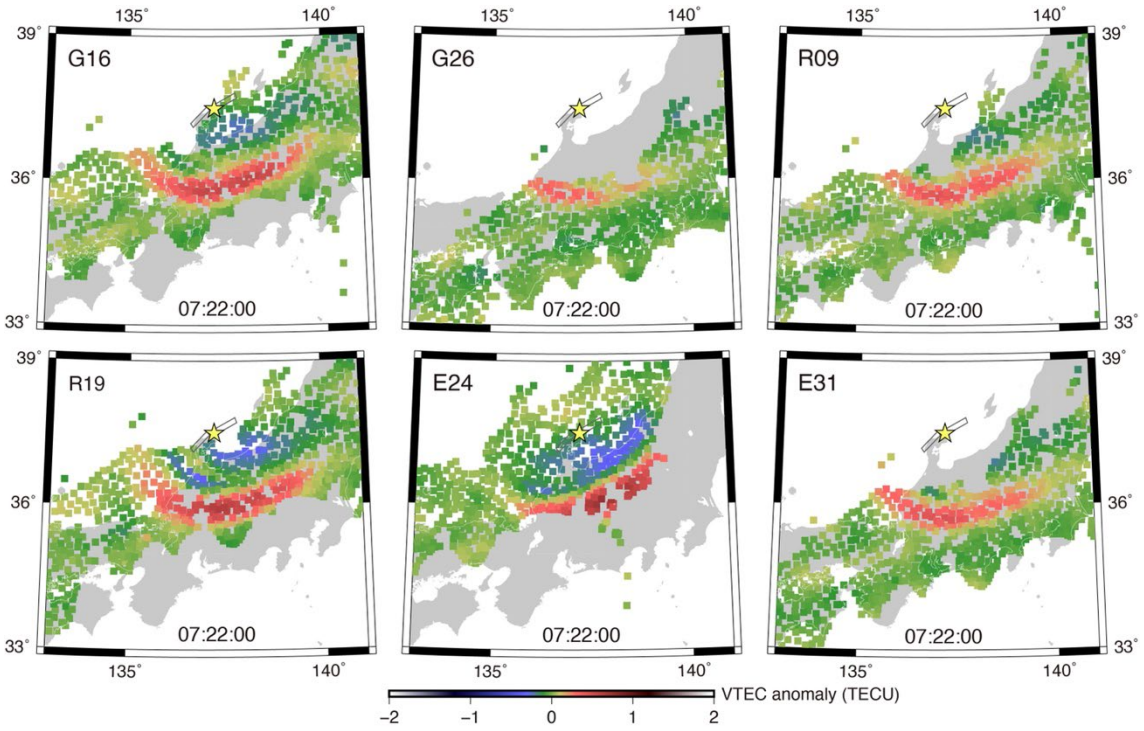

Fig. S5. Distribution of VTEC residuals with G16, G26, R09, R19, E24, and E31 satellites plotted on map for the same epoch 07:22. Similar residual maps drawn using J02 at six different epochs are given in Fig. 3. A thin ionosphere at altitude 300 km is assumed. By changing this altitude to 350 km, the positions of these dots may move by 10-20 km.

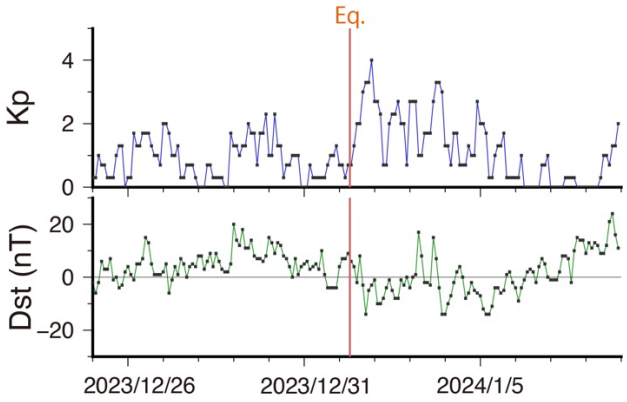

Fig. S6. Two indices (Kp and Dst), representing geomagnetic activities, over 15 days period encompassing the earthquake day (omniweb.nasa.gov). The 2024 Jan. 1 Noto-Peninsula earthquake occurred when the geomagnetic activity was relatively calm.